

First-principles calculation of the lattice thermal conductivities of α -, β -, and γ - Si_3N_4

Kazuyoshi Tatsumi,^{1,2,*} Atsushi Togo,² and Isao Tanaka^{2,3,4}

¹Advanced Measurement Technology Center, Institute of Materials and Systems for Sustainability, Nagoya University, Chikusa, Nagoya 464-8603, Japan

²Center for Elements Strategy Initiative for Structural Materials, Kyoto University, Sakyo, Kyoto 606-8501, Japan

³Department of Materials Science and Engineering, Kyoto University, Sakyo, Kyoto 606-8501, Japan

⁴Nanostructures Research Laboratory, Japan Fine Ceramics Center, Atsuta, Nagoya 456-8587, Japan

Lattice thermal conductivities of α -, β - and γ - Si_3N_4 single crystals are investigated from *ab-initio* anharmonic lattice dynamics, within the single-mode relaxation-time approximation of the linearized phonon Boltzmann transport equation. At 300 K, the lattice thermal conductivity of β - Si_3N_4 is calculated as $\kappa_{xx} = 73$ and $\kappa_{zz} = 198$ (in units of $\text{Wm}^{-1}\text{K}^{-1}$), that is consistent with the reported experimental values of 69 and 180, respectively. For α - Si_3N_4 , $\kappa_{xx} = 69$ and $\kappa_{zz} = 99$ are obtained. The difference of anisotropy between α - Si_3N_4 and β - Si_3N_4 is originated from their characteristic difference in the phonon band structures, although their crystal structures are similar in their local atomic coordinates. In α - Si_3N_4 , acoustic-mode phonons below 6 THz are the main heat carriers. In β - Si_3N_4 , the phonon modes up to 12 THz contribute to the lattice thermal conductivity. In γ - Si_3N_4 , $\kappa = 81$ is obtained. The distribution of phonon mode contributions to lattice thermal conductivity with respect to phonon frequency is found to closely resemble κ_{xx} of β - Si_3N_4 although the phonon lifetimes of γ - Si_3N_4 are twice shorter than those of β - Si_3N_4 .

I. INTRODUCTION

Several nitride insulators are known to exhibit high thermal conductivities and are important for heat transfer materials at elevated temperatures. For example, Slack *et al.*¹ reported that wurtzite-type w-AlN has thermal conductivity of $\gg 100 \text{ Wm}^{-1}\text{K}^{-1}$. Si_3N_4 has become another promising thermal conductive insulator as its thermal conductivity has been improved up to $177 \text{ Wm}^{-1}\text{K}^{-1}$ by using the advanced ceramic technologies related to the densification and microstructure control.²⁻⁵ Since the Si_3N_4 ceramics also exhibit high mechanical strength at elevated temperatures, they are regarded as ideal materials for the use in various applications, such as engine components, gas turbines, and heat sink substrates of power semiconductor devices.

At atmospheric pressure, Si_3N_4 exists in one of two phases, α and β , which are generally considered as low- and high-temperature phases, respectively.^{2,5,6} Their crystal structures belong to the space groups of P31c and P6₃/m, respectively.^{7,8} These structures have different stacking orders of equivalent basal layer structures originated by SiN_4 tetrahedra.⁹ In Fig.1 these layer structures are depicted from the principal direction, as A, B, C, and D in the α phase and A and B in the β phase. The stacking manners in α - and β - Si_3N_4 are thus as ABCDABCD.. and ABAB.., respectively. The α phase has additional two layer structures of C and D, which are related to the A and B by the *c* glide operation.⁹ Along this direction the lattice constant of the α phase is approximately two times longer than that of the β phase.

The reported values^{2-5,11} of the thermal conductivity of the Si_3N_4 polymorphs were measured on polycrystalline bulk samples. These values were significantly af-

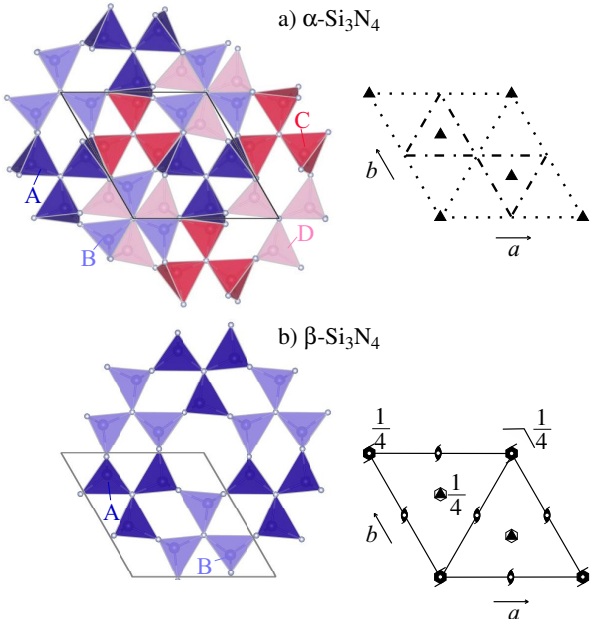


FIG. 1. (color online) Crystal structures of α - and β - Si_3N_4 . Stacking of SiN_4 tetrahedron layers are shown in left. (a) ABCDABCD.. for α - Si_3N_4 . (b) ABAB.. for β - Si_3N_4 . Space group diagrams¹⁰ in P31c (α - Si_3N_4) and P6₃/m (β - Si_3N_4) are shown in right.

fected by the contained lattice defects, impurities, shapes and orientations of the constituent crystal grains;¹² the thermal conductivity intrinsic to a defect-free single crystal has not been established. As an experimental access to the intrinsic thermal conductivity, Li *et al.*¹³ applied high-resolution thermoreflectance microscopy to a single β - Si_3N_4 grain in a ceramic sample. The analyzed

thermal conductivities were 69 and 180 Wm⁻¹K⁻¹ along the *a* and *c* axes, respectively. These thermal quantities correspond to the diagonal elements κ_{xx} and κ_{zz} of the lattice thermal conductivity tensor κ . We consider the anisotropy of $\kappa_{zz}/\kappa_{xx} \sim 3$ is relatively large. Theoretically, Hirosaki *et al.*¹² estimated κ by applying the Green-Kubo formulation to the molecular dynamics (MD) method with the interatomic potentials proposed by Vashishta *et al.*¹⁴. They calculated κ_{xx} and κ_{zz} of α -Si₃N₄ as 105 and 225 Wm⁻¹K⁻¹, and those of β -Si₃N₄ as 170 and 450 Wm⁻¹K⁻¹, respectively. The ratio κ_{zz}/κ_{xx} in β -Si₃N₄ agreed well with the experimental results obtained by Li *et al.*¹³: The κ_{ii} values overestimated the experimental by more than two times.

On many polymorphs of the wurtzite and zincblende structures, the lattice thermal conductivities were recently calculated based on a first principles calculation and Boltzman transport theory.¹⁵ These polymorphs have different stacking orders of the densest atom planes as ABAB.. and ABCABC... The different stacking orders merely altered the lattice thermal conductivities.¹⁵ The phonon linewidth distribution and phonon density of states were similar between the structures as well.¹⁵ On the other hand, the previous MD results on α - and β -Si₃N₄ presented that the different stacking orders in these phases altered the κ values largely. The large difference has not been clarified based on the microscopic phonon properties. It is interesting to investigate it using the same approach as in Ref.15 for α - and β -Si₃N₄.

In addition to the α and β phases, a cubic spinel phase (γ -Si₃N₄) is known to form upon compression and in-situ heating.^{16,17} The reported transition pressures were scattered from 10 to 36 GPa depending on the experimental conditions.¹⁸ The γ phase is experimentally quenched to atmospheric pressure at room temperature. Its thermal conductivity has not been experimentally reported; it has been estimated only by the Slack model.¹⁹

The present study aims to qualitatively understand the lattice thermal conductivity tensors among the three Si₃N₄ phases by means of the first principles approach. We calculate κ of the γ phase as well, for systematic understanding of the lattice thermal conductivity in the Si₃N₄ system. After the methodology section, we examine the validity of the present results first. Our calculated thermal properties are compared with the available experimental and theoretical references. Then we investigate the characteristics in the calculated κ in detail on the basis of the phonon band structures and phonon linewidths.

II. COMPUTATIONAL PROCEDURES

A. Lattice thermal conductivity calculation

The lattice thermal conductivities were calculated by solving the linearized Boltzmann transport equation (LBTE) within the single-mode relaxation time approx-

imation (single-mode RTA). We also tried the direct solution of LBTE²⁰ and leave its calculated κ values in the following section. The difference in the calculated κ between by the single-mode RTA and by the direct solution was found minor for our discussion. Therefore we limited our research to use the single-mode RTA to take advantage of its intuitive closed form of κ .

In the following sections, we denote a phonon mode by $\lambda = (\mathbf{q}, p)$ with the set of the phonon wave vector \mathbf{q} and band index p and $-\lambda \equiv (-\mathbf{q}, p)$. The relaxation time due to phonon-phonon scattering was obtained as reciprocal of linewidth, $\tau_{\lambda,ph-ph} = (2\Gamma_{\lambda})^{-1}$, where the linewidth that we employed in this study is as follows:

$$\begin{aligned} \Gamma_{\lambda} = & \frac{18\pi}{\hbar^2} \sum_{\lambda'\lambda''} |\Phi_{-\lambda\lambda'\lambda''}|^2 \times \\ & \{(n_{\lambda'} + n_{\lambda''} + 1)\delta(\omega_{\lambda} - \omega_{\lambda'} - \omega_{\lambda''}) + \\ & (n_{\lambda'} - n_{\lambda''})[\delta(\omega_{\lambda} + \omega_{\lambda'} - \omega_{\lambda''}) - \delta(\omega_{\lambda} - \omega_{\lambda'} + \omega_{\lambda''})]\}. \end{aligned} \quad (1)$$

Here ω_{λ} is the harmonic phonon frequency of the phonon mode λ , $n_{\lambda} = [\exp(\hbar\omega_{\lambda}/k_B T) - 1]^{-1}$ is the Bose-Einstein distribution at temperature T , and $\Phi_{\lambda\lambda'\lambda''}$ denotes the three-phonon-scattering strength. $\Phi_{\lambda\lambda'\lambda''}$ was obtained by usual coordinate transformation of third-order force constants from direct space to phonon space.¹⁵ The second- and third-order real-space force constants were obtained from the *ab-initio* calculation, whose details are written in the next section.

In order to compare the more realistic results of the calculated κ with the experimental data, the isotopic scattering effect due to the natural isotope distribution was taken into account according to the second-order perturbation theory.²¹ With the relaxation times of the phonon-phonon scattering and isotopic scattering, $\tau_{\lambda,ph-ph}$ and $\tau_{\lambda,iso}$, the total relaxation time for a phonon mode was assumed to be $1/\tau_{\lambda} = 1/\tau_{\lambda,ph-ph} + 1/\tau_{\lambda,iso}$, according to Matthiessen's rule.

The available experimental thermal conductivity data of the Si₃N₄ system have been measured on the polycrystalline samples and not measured from any single crystals. In order to consider the effect of various lattice defects in the polycrystalline samples, such as grain boundaries, impurities, and vacancies, we crudely took them into account by a relaxation time $\tau_{\lambda,bs} = L/|\mathbf{v}_{\lambda}|$ of a phonon boundary scattering model, where $\mathbf{v}_{\lambda} = \nabla_{\mathbf{q}}\omega_{\lambda}$ is the group velocity and L a parameter regarding to the boundary mean free path. We consider $\tau_{\lambda,bs}$ as a variable parameter and included it to κ according to Matthiessen's rule.

The closed form of κ within RTA was obtained via

$$\kappa(T) = \frac{1}{N_{\mathbf{q}}\Omega} \sum_{\lambda} \tau_{\lambda}(T) \mathbf{v}_{\lambda} \otimes \mathbf{v}_{\lambda} c_{\lambda}(T), \quad (2)$$

where $N_{\mathbf{q}}$ is the number of \mathbf{q} -points, Ω is the unit cell volume, and c_{λ} is the mode heat capacity. To analyze κ in

detail, we calculate the cumulative thermal conductivity:

$$\kappa^c(\omega) = \frac{1}{N_q\Omega} \int_0^\omega \sum_\lambda \tau_\lambda(T) \mathbf{v}_\lambda \otimes \mathbf{v}_\lambda c_\lambda(T) \delta(\omega' - \omega) d\omega', \quad (3)$$

and its derivative $\frac{\partial \kappa^c(\omega)}{\partial \omega}$ to see the phonon mode contributions to κ .

The lattice thermal conductivities were calculated with the phonon-phonon interaction calculation code PHONO3PY¹⁵, while the harmonic phonon states were analyzed with the phonon calculation code PHONOPY²².

B. Computational details

The force constants were calculated using the first-principles projector augmented wave method²³ (VASP code^{24–26}). The generalized gradient approximation (GGA) parameterized by Perdew, Burke, and Ernzerhof²⁷ was used for the exchange correlation potential. A plane wave energy cutoff of 500 eV was employed. The crystal structures were optimized until the residual forces acting on the constituent atoms was less than 10^{-6} eV/Å. The structural optimization was firstly performed for a temperature of 0 K and 0 GPa. Here the temperature and pressure were considered only for the electronic system and the zero point lattice vibration was not taken into account. The calculated lattice parameters were $a = 7.808$ Å and $c = 5.659$ Å for the α phase, $a = 7.660$ Å and $c = 2.925$ Å for the β phase, and $a = 7.787$ Å for the γ phase, which agree with the experimental data^{7,8,28} within +0.7 % errors. The lattice volume optimized within the local density approximation (LDA)²⁹ for the exchange correlation potential was, for $\beta\text{-Si}_3\text{N}_4$, 3 % smaller than within GGA, which is a typical volume contraction of LDA. The κ calculated within LDA was larger by 2.6 % than within GGA. For our discussion, this difference is enough small, therefore the impact of choice of exchange correlation potential is considered to be minor in our study.

Supercell and finite difference approaches were used to calculate the force constants.³⁰ The supercells were $1 \times 1 \times 2$, $1 \times 1 \times 3$, and $1 \times 1 \times 1$ supercells of the conventional unit cells for the calculation of the third-order force constants in α , β , and $\gamma\text{-Si}_3\text{N}_4$, respectively; they were $3 \times 3 \times 4$, $3 \times 3 \times 8$ and $2 \times 2 \times 2$ for the second-order force constants. The length of the induced atomic displacement was set to 0.03 Å. Table I shows the κ calculated with several different sets of the supercells, indicating that our calculated κ is reasonably converging with respect to the size of the supercells.

Non-analytical term correction³¹ was applied to the second-order force constants to take into account the long range Coulomb forces present in ionic crystals. For the correction, Born effective charges were calculated by using the density functional perturbation theory

TABLE I. Calculated lattice thermal conductivities of α -, β -, and $\gamma\text{-Si}_3\text{N}_4$ ($\text{WK}^{-1}\text{m}^{-1}$) at 300 K with respect to several combinations of supercell sizes.

Phase	Supercell (# of atoms)		LTC	
	3 rd force constants	2 nd force constants	<i>xx</i>	<i>zz</i>
α	1 \times 1 \times 1 (28)	1 \times 1 \times 1 (28)	37	57
	1 \times 1 \times 2 (56)	1 \times 1 \times 2 (56)	41	79
	1 \times 1 \times 1 (28)	2 \times 2 \times 2 (224)	55	81
	1 \times 1 \times 2 (56)	2 \times 2 \times 2 (224)	67	95
	1 \times 1 \times 2 (56)	2 \times 2 \times 3 (336)	68	97
	1 \times 1 \times 2 (56)	3 \times 3 \times 4 (1008)	68	100
β	1 \times 1 \times 2 (28)	1 \times 1 \times 2 (28)	44	173
	1 \times 1 \times 2 (28)	2 \times 2 \times 4 (224)	76	208
	1 \times 1 \times 3 (42)	2 \times 2 \times 4 (224)	71	194
	1 \times 1 \times 3 (42)	2 \times 2 \times 5 (280)	72	196
	1 \times 1 \times 3 (42)	3 \times 3 \times 8 (1008)	73	199
γ	1 \times 1 \times 1 (56)	1 \times 1 \times 1 (56)	72	
	1 \times 1 \times 1 (56)	2 \times 2 \times 2 (448)	77	
	1 \times 1 \times 1 (56)	3 \times 3 \times 3 (56)	79	

(DFPT).Ref!

Uniform \mathbf{k} -point sampling meshes of $4 \times 4 \times 2$, $4 \times 4 \times 3$, and $3 \times 3 \times 3$ were used for the third-order force constants of the α , β , and γ phases. For the α and β phases the center of the $a^* \text{-} b^*$ plane was sampled while the center on the c^* -axis was not. For the γ phase, non- Γ center mesh was used. For the second-order force constants, the Γ -point was only sampled for the α and β phase and the only one $\mathbf{k} = (0.5, 0.5, 0.5)$ point was sampled for the γ phase. The \mathbf{q} -point sampling meshes of $10 \times 10 \times 14$, $10 \times 10 \times 26$, and $12 \times 12 \times 12$ were used to calculate κ in Eq. (2) for the α , β , and γ phases.

We examined the effect of thermal expansion on κ by calculating them with the crystal structures optimized for several finite temperatures within the quasi-harmonic approximation (QHA)³². The structure was optimized for a temperature and 0 GPa so as to show a minimum Helmholtz free energy. κ for the temperature was calculated with the optimized structure. This κ was differed from the one for the temperature, calculated with the structure optimized for 0 K and 0 GPa. We consider that this difference is caused by the thermal expansion of the lattice. For $\beta\text{-Si}_3\text{N}_4$ and the temperatures of 300, 600, 900, 1200, and 1500 K, the differences in κ between the two structures were found less than 1 %, similar to the case of Si and Ge³³. For the present study, these differences are negligible and we adopt the κ calculated with the structure optimized for 0 K and 0 GPa.

We calculated the volumetric thermal expansion coefficients and compared them with the reported experimental values so as to check the validity of the present thermal conductivity calculation, because the thermal expansion is originated from the anharmonicity of the interatomic potential as well as κ . The calculated val-

ues of the α and β phases are 4.31×10^{-6} and $4.19 \times 10^{-6} \text{ K}^{-1}$ for 300 K, while the experimental values³⁴ were 3.75×10^{-6} and $3.55 \times 10^{-6} \text{ K}^{-1}$. The present calculation reproduced the experimental tendency where the α phase has a slightly larger thermal expansion coefficient than the β phase, supporting that the present calculations enable us to qualitatively compare the calculated κ of the Si_3N_4 phases.

In order to compare the microscopic phonon properties among the three phases at the same conditions, those results calculated at 0 GPa are shown and discussed. For the γ phase, this means that we assume the condition of a virtually quenched γ phase at 0 GPa from the high pressure. To examine the analytical continuity of the properties with respect to pressures, we calculated κ of the γ phase at 10, 20, and 40 GPa as shown in Fig. 8. The phenomenological behaviour of linear dependence of κ with respect to pressure was reproduced as similar to Ref. 35. The slope was $2.89 \text{ Wm}^{-1}\text{K}^{-1}\text{GPa}^{-1}$ for the γ phase. By this dependence, we consider that the microscopic values are also varied smoothly with the pressure and those at 0 GPa are valuable to compare with the α and β phases.

C. Direct solution of LBTE

The merit to employ the single-mode RTA for thermal conductivity calculation is the closed form, by which we can intuitively understand the qualitative character of κ in terms of the relaxation time and group velocity. The microscopic understanding of the full solution of LBTE is still under the development³⁶ and the microscopic picture based on collective phonons³⁷ will require more complicated investigation although it is known that the single-mode RTA solution of LBTE often underestimates the full solution.^{33,38}

On the κ of the α and β phases, we adopted a direct solution of LBTE²⁰, which is one of the methods of LBTE full solutions. Their κ_{xx} and κ_{zz} without the isotope effect were 69 and $102 \text{ Wm}^{-1}\text{K}^{-1}$ for the α phase and 76 and $238 \text{ Wm}^{-1}\text{K}^{-1}$ for the β phase, respectively, while the corresponding single-mode RTA values were 70 and $102 \text{ Wm}^{-1}\text{K}^{-1}$ for the α phase and 76 and $210 \text{ Wm}^{-1}\text{K}^{-1}$ for the β phase. The κ_{zz} of the direct solution in the β phase was 13 % larger than that of the single-mode RTA solution. Since the differences in κ between the LBTE solutions are not significant, we expect the physics on those lattice thermal conductivities is well understood within RTA in the current level of our interest. **Therefore, we discuss the lattice thermal conductivities using the results of the single-mode RTA solution.**

TABLE II. Calculated thermal conductivities of $\alpha\text{-Si}_3\text{N}_4$ (trigonal), $\beta\text{-Si}_3\text{N}_4$ (trigonal), and $\gamma\text{-Si}_3\text{N}_4$ (cubic) at 300 K, compared with the experimental data. Theoretical bulk moduli B in units of GPa, calculated by the authors by using the present band method, are presented in the fourth column.

	This work		κ	Ref. Theo.		Ref. Expt.	
	κ_{xx}	κ_{zz}		κ_{xx}	κ_{zz}	κ_{xx}	κ_{zz}
$\alpha\text{-Si}_3\text{N}_4$	68	100	224	70 ^a	105 ^b	225 ^b	-
$\beta\text{-Si}_3\text{N}_4$	73	199	237	250 ^a	170 ^b	450 ^b	69 ^c 180 ^c
$\gamma\text{-Si}_3\text{N}_4$	77	-	296	80 ^a	-	-	-

^a Ref. 19, Slack model.

^b Ref. 12, molecular dynamics (Green-Kubo).

^c Ref. 13, single crystalline grains of poly-crystals.

III. RESULTS AND DISCUSSION

A. Lattice thermal conductivities

Table II shows the present results of the κ for 300 K. $\beta\text{-Si}_3\text{N}_4$ has markedly more anisotropic κ than $\alpha\text{-Si}_3\text{N}_4$. The directional averages $\sum_i \kappa_{ii}/3$ are 79, 115, and 77 $\text{Wm}^{-1}\text{K}^{-1}$ for the α , β , and γ phases, respectively. The value of the γ phase is similar to that of the α phase, in spite of comparatively large difference among the bulk moduli (B) that are also shown in Table II.

Table II also shows the previously reported experimental¹³ and theoretical¹² thermal conductivities for the references. Previously Morelli *et al.*¹⁹ employed the Slack model for estimating the lattice thermal conductivities of the three phases. They are shown as κ in Table II. For the β phase, our κ agrees better with the experimental, than that of the molecular calculation¹² does. Also, our directional average $\sum_i \kappa_{ii}/3$ ($115 \text{ Wm}^{-1}\text{K}^{-1}$) agrees better with the experimental average ($106 \text{ Wm}^{-1}\text{K}^{-1}$), than the Slack model does.

Fig. 2 shows the theoretical κ of the α and β phases as a function of T , together with the reference experimental data^{5,11,13}. The thermal conductivities for a series of temperatures were only reported on the polycrystalline bulk samples. These bulk thermal conductivities cannot be directly compared with the calculated intrinsic κ because the microstructures of the bulk samples largely affected the bulk thermal conductivities: They were deviated from the simple directional averages of the intrinsic κ_{ii} , depending on the shapes of the constituent crystal grains. We treated this effect by using a parameter $0 \leq w \leq 1$ and fitting quantities of $w\kappa_{xx} + (1-w)\kappa_{zz}$ to the experimental bulk thermal conductivities by the least squares method. We consider these as theoretical bulk thermal conductivities

In Fig. 2, the κ_{ii} calculated without $\tau_{\lambda,\text{bs}}$ are nearly proportional to T^{-1} because n_λ in Eq. (1) can be reduced to $\exp(-\hbar\omega_\lambda/k_B T)$. In Fig. 2-a, the temperature dependence of the experimental bulk thermal conductivities of a chemically vapor-deposited $\alpha\text{-Si}_3\text{N}_4$ sample¹¹ is

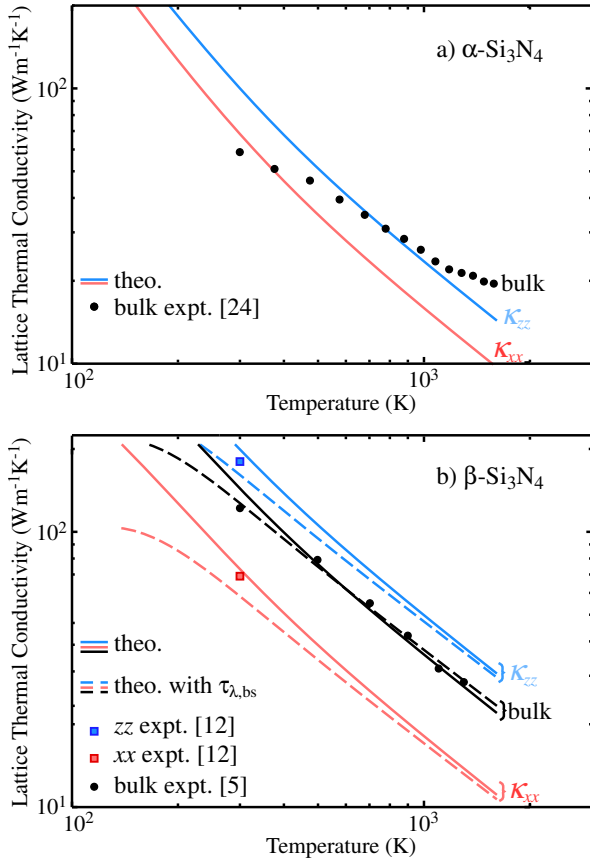


FIG. 2. (color online) Temperature dependence of thermal conductivities for α - and $\beta\text{-Si}_3\text{N}_4$. For $\beta\text{-Si}_3\text{N}_4$, theoretical results with the boundary scattering effect are shown by broken lines. Theoretical bulk thermal conductivities (see in text) for the $\beta\text{-Si}_3\text{N}_4$ sample are also shown to be compared with the experimental bulk thermal conductivities.

deviated from inverse proportion considerably, intersecting the theoretical lines. Thus no value of w adjusts the theoretical conductivities to the experimental data. The full solution of LBTE would negligibly cure the disagreement. Including the simple phonon lifetime of boundary scattering, $\tau_{\lambda,\text{bs}} = L/|\mathbf{v}_{\lambda}|$, into the total phonon lifetime according to Matthiessen's rule, could not explain the discrepancy as well. A L value of $0.6 \mu\text{m}$, which was much smaller than the experimental grain size¹¹ of $10 \mu\text{m}$, decreased the room-temperature theoretical κ_{xx} and κ_{zz} values toward the experimental values, but severely underestimated the experimental values in the high temperature side. At present, the reason for the discrepancy between the theoretical and experimental behaviors is unclear. Although the crystal structure of the experimental sample was characterized as $\alpha\text{-Si}_3\text{N}_4$, significant lattice defects might exist in the as-deposited sample as pointed out by Hirosaki *et al.*¹² and the simple phonon boundary scattering model might fail to describe their effects on the bulk thermal conductivities.

The experimental bulk thermal conductivities of the β

phase are located in-between the theoretical κ_{xx} and κ_{zz} , being nearly proportional to T^{-1} . Simple directional averages of the theoretical κ_{ii} slightly underestimate these experimental values. This is understood from the fact that the microstructure was controlled to improve the thermal conductivity, and the crystalline grains were selectively grown along the c axis of the most conductive direction.⁵ The theoretical bulk thermal conductivities were fit well with $w = 0.44$ to the experimental bulk thermal conductivities. For the effects of lattice defects most of which were grain boundaries, we included $\tau_{\lambda,\text{bs}}$ with $L = 0.6 \mu\text{m}$ to further fit the theoretical curve ($w = 0.33$) to the experimental data. The L value is slightly smaller than the average grain size⁵ ($2 \mu\text{m}$) of the experiment. The experimental κ_{ii} are rather close to the theoretical κ_{ii} calculated without $\tau_{\lambda,\text{bs}}$. This is explained by the fact that the experimental κ_{xx} and κ_{zz} were deduced consistently through the grains of several different sizes. The effects of the phonon scattering at the grain boundaries were eliminated.¹³

B. Dispersion curves

Figure 3 shows the phonon band diagrams of the three Si_3N_4 phases. The entire band diagrams are almost identical to those reported earlier^{18,39}. However, here we investigate the group velocities projected on the high-symmetry paths, especially focusing on their anisotropy of the α and β phases. This was not investigated by the previous works.

The ω_{λ} on the acoustic branches in the β phase increase much more from Γ to A than from Γ to K or M . In the α phase, the corresponding ω_{λ} increase more equally among the paths. This difference is due to the different $\Gamma\text{-}A$ path lengths. The β phase has an approximately twice longer path than the α phase; the lattice constant c of the β phase is nearly half that of the α phase, owing to the difference in the stacking manner of the basal layers. Normally, optical branches are flat; however, the upper branches along the $\Gamma\text{-}A$ path also have significantly large gradients in the β phase. These findings indicate that the β phase contains a larger number of phonon modes whose $v_{\lambda,z}$ is large and whose \mathbf{v}_{λ} orients to the c axis direction. We will show this tendency further in the following sections.

In the γ phase, the acoustic phonon branches show significant linear dispersions on the $\Gamma\text{-}L$ and $\Gamma\text{-}X$ paths. The roughly constant gradients of ω_{λ} are large, reflecting the large elastic constants of the γ phase as shown in Table II.

C. ω_{λ} counter map on reciprocal plane

We show the anisotropy in the group velocities on another geometry, that is, a cross-section of the Brillouin-zone. In Fig. 4, we show the distributions on the $b^*\text{-}c^*$



FIG. 3. (color online) Brillouin-zones (left) and calculated phonon band diagrams (right) for three Si_3N_4 phases.

plane. The distributions for four bands from the lowest frequency are shown, because these bands contribute significantly to the κ . We did not find any significant differences in the distributions between the b^*-c^* plane and the other planes containing the c^* axis. Thus we select the b^*-c^* plane as a representative plane. In the α phase, the distributions are nearly isotropic. Their gradients, the group velocities projected onto the b^*-c^* plane, are thus nearly isotropic. On the other hand, in the β phase, the iso-frequency lines in $0.06 \leq q_{c^*} \leq 0.12 \text{ \AA}^{-1}$ are rather parallel to the q_{b^*} axis, confirming that the four bands of the β phase, in a significantly large part of the Brillouin zone, have \mathbf{v}_λ oriented to the c axis direction.

D. Frequency-dependences of κ^c , \mathbf{v}_λ and Γ_λ

We have investigated in the previous two sections the anisotropy in the \mathbf{v}_λ for obtaining an insight on the anisotropy in the κ . Here we completely investigate the characteristic points in the κ by using the important phonon properties existing in the closed form of RTA

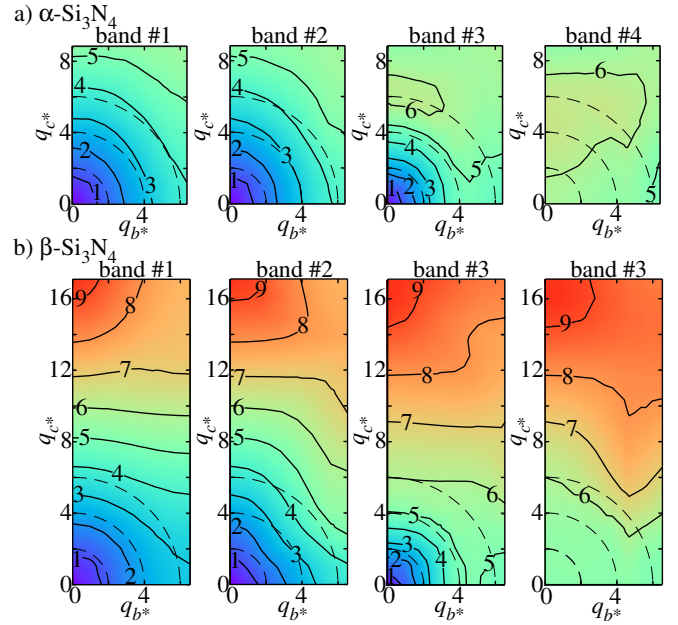


FIG. 4. (color online) Contour maps of phonon frequency (THz) on the b^*-c^* planes of Brillouin-zones. The coordination in the reciprocal plane are in units of 10^{-2} \AA^{-1} . The maps for the four lowest-frequency phonon states are shown. The frequency landscapes are formed by simply connecting the frequencies of the same band indices, assigned by ascending order of frequency at the respective \mathbf{q} points.

in Eq. (2). These properties are taken over the Brillouin zone because the κ is a quantity integrated there. In order to visually show the similarity or differences in these properties among the phases, we plot in Fig. 5 the frequency distribution of the properties: The phonon density of states (DOS) shows the distribution of the heat carriers. The cumulative thermal conductivities κ^c show the phonon frequencies where the phonons largely contribute to the κ . Their 1st derivatives are also shown to clearly identify the frequencies. By weighting the DOS with $v_{\lambda,i}^2$, we show the impacts of the $v_{\lambda,i}$ and carrier density together. We abbreviate these weighted DOS as WDOS. The phonon linewidth is the remaining important property. Scatter plots of $(\Gamma_\lambda, \omega_\lambda)$ are employed to compare their impacts.

The distinct first peaks in the DOS are indicated by arrows in Fig. 5-a. They are crudely related to the flattening of the acoustic branches near the Brillouin zone boundaries. It is interesting that only κ^c in the β phase increase significantly in the frequency range beyond the peak. This is due to the anisotropic dispersions of the acoustic phonon branches and the large gradients of the low frequency optical phonon branches.

Compared the four kinds of phonon properties among the three phases, the DOS, WDOS and Γ_λ distribution of the γ phase are much different from the other phases. These large differences are consistent with the large differences in the crystal structure. We do not investi-

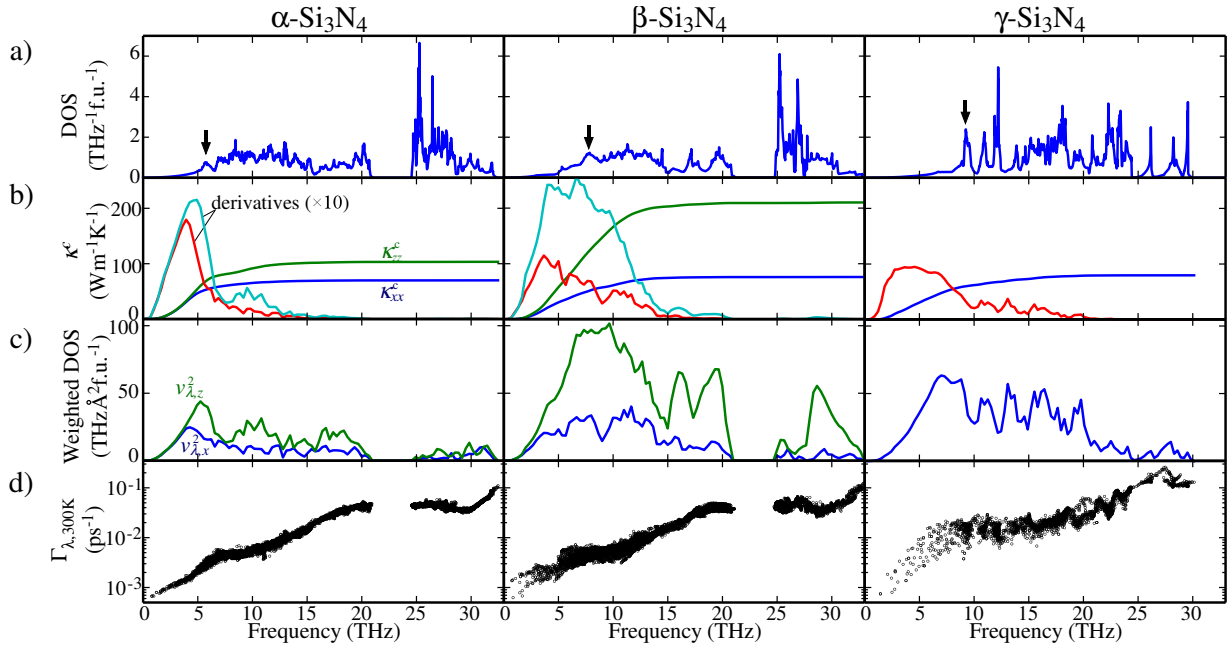


FIG. 5. (color online) Microscopic phonon properties of three Si_3N_4 phases. Cumulative thermal conductivity κ^c and its derivative (a), DOS (b), weighted DOS with $v_{\lambda,i}^2$ (c) and linewidth Γ_λ (d).

gate further details of them in the present study. The linewidths of the γ phase are nearly twice larger than those of the α and β phases in the frequency range where the derivative of the κ^c is large. The WDOS in the γ phase is larger than the other phases in the most part of the frequency range. As a result of the opposite impacts of these two properties, the κ_{xx}^c of the γ phase resembles closely to κ_{xx}^c of the β phase.

We hereafter focus on the comparison between the α and β phases. As for the anisotropy in the κ , we find clear similarity between $\frac{d\kappa_{ii}^c}{d\omega_\lambda}$ and WDOS with $v_{\lambda,i}^2$. The remaining property, linewidth distributions are similar between the phases. The DOS are also similar. Therefore, the \mathbf{v}_λ simply account for the difference in the κ anisotropy between the two phases.

It is still curious that the linewidths are similar between these phases although their group velocities have marked differences. Thus we investigate this similarity further. Previously, Lindsay *et al.* have pointed out a significant positive correlation between LTC and phase space available for the three-phonon scattering according to the selection rules due to the momentum and energy conservation for the three-phonon processes.⁴⁰ More recently Togo *et al.* have shown that the frequency profiles of the imaginary part of self-energy $\Gamma_\lambda(\omega)$, where $\Gamma_\lambda(\omega_\lambda) = \Gamma_\lambda$, are characterized by the three phonon selection rules.¹⁵ In Eq. (1) of the linewidths, $\Phi_{-\lambda\lambda'\lambda''}$ partly contains the selection rule due to the momentum conservation.⁴¹ In the present study, we examine the impacts on the linewidths of $\Phi_{-\lambda\lambda'\lambda''}$ and the whole selection rules, one by one.

In Table. III, the magnitudes of $\Phi_{-\lambda\lambda'\lambda''}$ are compared as the averages over the ω_λ frequency ranges between 0–15 and 0–35 THz and over all λ' and λ'' . The values of the α and β phases are very close to each other, indicating that $\Phi_{-\lambda\lambda'\lambda''}$ have similar impacts.

TABLE III. Averages of $\Phi_{-\lambda\lambda'\lambda''}$ over frequency ranges of ω_λ (0–15 and 0–35 THz) and all (λ', λ') . The values are in units of $10^{-10} \text{ eV}^2 \text{f.u.}^{-1}$.

Frequency Range (THz)	Phase		
	α	β	γ
0–15	2.66	2.63	5.76
0–30	13.1	13.0	11.4

In order to analyze the impacts of the selection rules on the linewidths, we employ the joint density of states (JDOS) $D_2(\mathbf{q}, \omega)$,

$$D_2(\mathbf{q}, \omega) = D_2^{(1)}(\mathbf{q}, \omega) + D_2^{(2)}(\mathbf{q}, \omega) \quad (4)$$

where

$$\begin{aligned} D_2^{(1)} &= \frac{1}{N} \sum_{\lambda' \lambda''} \Delta(-\mathbf{q} + \mathbf{q}' + \mathbf{q}'') \\ &\times [\delta(\omega + \omega_{\lambda'} - \omega_{\lambda''}) + \delta(\omega - \omega_{\lambda'} + \omega_{\lambda''})], \\ D_2^{(2)} &= \frac{1}{N} \sum_{\lambda' \lambda''} \Delta(-\mathbf{q} + \mathbf{q}' + \mathbf{q}'') \\ &\times \delta(\omega - \omega_{\lambda'} - \omega_{\lambda''}), \end{aligned}$$

with $\Delta(\mathbf{x})$ giving 1 if \mathbf{x} is a reciprocal lattice vector and otherwise zero.

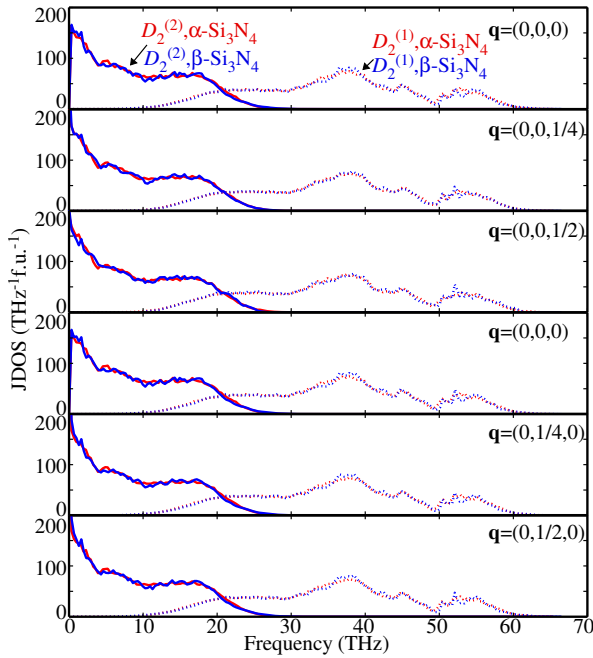


FIG. 6. (color online) JDOS of α - and γ - Si_3N_4 at different \mathbf{q} points. The first and forth rows are JDOS at the same Γ -point but calculated with the polarization for non-analytic term correction set along c^* and b^* , respectively.

Fig. 6 shows the frequency-dependences of JDOS at different \mathbf{q} -points on the Γ -A and Γ -K paths, which show very slight \mathbf{q} -point dependence. Eq. (1) includes Bose-Einstein functions for the involved phonon modes and JDOS can be weighted with them as done in refs. 15 and 38, however we omit them for simplicity. With the weights, the absolute values are affected but the weighted JDOS of the α and β phases are still similar. At the low frequency region responsible for the LTCs, among the two terms of $D_2^{(1)}$ and $D_2^{(2)}$ in Eq. (4), dominant is $D_2^{(2)}$ which basically corresponds to the half part ($\omega \geq 0$) of the auto-correlation function of DOS, which, for the α and β phases, commonly show the frequency gap (Fig. 5-a). $D_2^{(2)}$ curves reflect this DOS feature, dropping suddenly around 0 THz and showing a small shoulder around 5 THz, which corresponds to the width of the gap. Moreover $D_2^{(2)}$ shows a broad peak around 18 THz, which corresponds to the frequency shift to make the largest correlation between the higher and lower portions of DOS across the gap. Because the gap is basically originated from the differences in the vibrations of the planer NSi_3 commonly contained in the α and β phases³⁹, the major shapes of $D_2^{(2)}$, reflecting this gap feature, are similar in these phases. With the same origin, the JDOS of $D_2^{(1)}$ are also similar in these phases. With these similar impacts of $\Phi_{-\lambda\lambda'\lambda''}$ and JDOS on Γ_λ , Γ_λ in Fig. 5-d are similar.

As a small but interesting difference in the linewidths between these phases, Γ_λ below 5 THz in Fig. 5-d are aligned on a smooth line in the α phase, while those in

the β phase are scattered roughly onto two different lines. This difference can be explained by the vibration directions shown in Fig. 7. In Fig. 7-a, Γ_λ are classified using colors according to the sums of the squares of the eigenvector components along \mathbf{q} ; the sum is 1 for perfectly longitudinal waves. However, these sums have no clear contrast to distinguish the two branches in the β phase. Fig. 7-b shows the same plot as Fig. 7-a, but with colors according to the sums of the squares of the eigenvector components along the a - b plane, which has 1 when the eigenvectors lie on the a - b plane. There is a tendency in the β phase that Γ_λ are large for the vibrations along the a - b plane. Therefore, within the single-mode RTA, for the phonon modes below 5 THz, all of which belong to the acoustic phonon branches, the vibration modes along the a - b plane are more easily scattered in the β phase, no matter whether they are longitudinal or transverse. For the panel of β - Si_3N_4 in Fig. 7-b, a straight line can divide the phonon modes into the two groups. The numbers of the phonon modes in the upper and lower parts are 157 and 58, whose ratio is rational as the population ratio of the vibration modes along and out of the a - b plane.

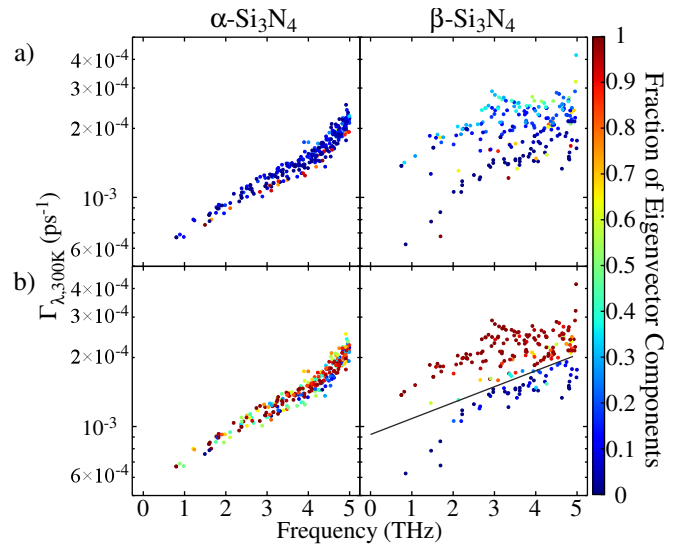


FIG. 7. (color online) Distribution of linewidths $\omega_\lambda \leq 5$ THz with colormaps with respect to strengths of eigenvector components along \mathbf{q} (a) and on a - b plane (b).

IV. SUMMARY

In the present study, we investigate the lattice thermal conductivities of the three Si_3N_4 phases, by using the lattice dynamics based on the *ab-initio* interatomic force constants. The main remarks are as follows:

1) In the α - and β - Si_3N_4 , whose crystal structures are characterized by the stacking manners of the basal layers, which alter the LTCs. In α - Si_3N_4 , the LTC tensors are rather isotropic, while κ_{zz} of the β phase is much larger

than the others, showing remarkable anisotropy in the LTC tensor.

2) In the α phase, the acoustic mode phonons below 6 THz are the main heat carriers, while in the β phase, the phonons below 12 THz contribute to the thermal conductivity. Their group velocities are significantly different between the phases; their linewidths are basically similar due to the similar impacts of the phonon-phonon interaction strengths and selection rules. Therefore the difference in the group velocities alone qualitatively explains the difference of anisotropy.

3) In the γ phase, the frequency distribution of the phonon mode contributions to LTC is found to be similar to that for κ_{xx} of $\beta\text{-Si}_3\text{N}_4$ although the respective phonon properties (group velocities and linewidths) are much different from those of the other phases

ACKNOWLEDGMENTS

The present work was partly supported by Grants-in-Aid for Scientific Research of MEXT, Japan (Grant No. 15K14108 and ESISM (Elements Strategy Initiative for Structural Materials) of Kyoto University).

Appendix A: Pressure dependence of LTC of γ -phase

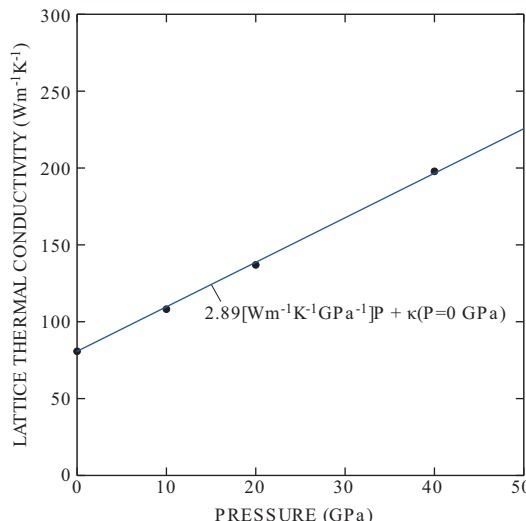


FIG. 8. (color online) Pressure dependence of LTC of $\gamma\text{-Si}_3\text{N}_4$.

^{*} k-tatsumi@imass.nagoya-u.ac.jp

¹ G. Slack, Journal of Physics and Chemistry of Solids **34**, 321 (1973).

² Y. Zhou, H. Hyuga, D. Kusano, Y.-i. Yoshizawa, and K. Hirao, Advanced Materials **23**, 4563 (2011).

³ K. Hirao, K. Watari, H. Hayashi, and M. Kitayama, MRS Bulletin **26**, 451 (2001).

- ⁴ K. Watari, Journal of the Ceramic Society of Japan **109**, S7 (2001).
- ⁵ N. Hirosaki, Y. Okamoto, M. Ando, F. Munakata, and Y. Akimune, Journal of the Ceramic Society of Japan **104**, 49 (1996).
- ⁶ F. L. Riley, Journal of the American Ceramic Society **83**, 245 (2000).
- ⁷ M. Yashima, Y. Ando, and Y. Tabira, The Journal of Physical Chemistry B **111**, 3609 (2007).
- ⁸ D. Du Boulay, N. Ishizawa, T. Atake, V. Streltsov, K. Furuya, and F. Munakata, Acta Crystallographica Section B: Structural Science **60**, 388 (2004).
- ⁹ S. Hampshire, H. Park, D. Thompson, and K. Jack, Nature **274**, 880 (1978).
- ¹⁰ T. Hahn, ed., International tables for crystallography, Vol. A (John Wiley & Sons, Inc., 2011).
- ¹¹ T. Hirai, S. Hayashi, and K. Niihara, AM. CERAM. SOC. BULL. Am. Ceram. Soc. Bull. **57**, 1126 (1978).
- ¹² N. Hirosaki, S. Ogata, C. Kocer, H. Kitagawa, and Y. Nakamura, Physical Review B **65**, 134110 (2002).
- ¹³ B. Li, L. Pottier, J. Roger, D. Fournier, K. Watari, and K. Hirao, Journal of the european ceramic society **19**, 1631 (1999).
- ¹⁴ R. Vashishta, R. K. Kalia, A. Nakano, and I. Ebbsö, Amorphous Insulators and Semiconductor, edited by M. F. Thorpe and M. I. Mitkova (Kluwer, 1996).
- ¹⁵ A. Togo, L. Chaput, and I. Tanaka, Physical Review B **91**, 094306 (2015).
- ¹⁶ A. Zerr, G. Miehe, G. Serghiou, M. Schwarz, E. Kroke, R. Riedel, H. Fueß, P. Kroll, and R. Boehler, Nature **400**, 340 (1999).
- ¹⁷ Y. Zhang, A. Navrotsky, and T. Sekine, Journal of materials research **21**, 41 (2006).
- ¹⁸ B. Xu, J. Dong, P. F. McMillan, O. Shebanova, and A. Salamat, Physical Review B **84**, 014113 (2011).
- ¹⁹ D. Morelli and J. Heremans, Applied physics letters **81**, 5126 (2002).
- ²⁰ L. Chaput, Physical review letters **110**, 265506 (2013).
- ²¹ S.-i. Tamura, Physical Review B **27**, 858 (1983).
- ²² A. Togo and I. Tanaka, Scripta Materialia **108**, 1 (2015).
- ²³ P. E. Blöchl, Phys. Rev. B **50**, 17953 (1994).
- ²⁴ G. Kresse and J. Furthmüller, Physical review B **54**, 11169 (1996).
- ²⁵ G. Kresse, J. Non-Cryst. Solids **193**, 222 (1995).
- ²⁶ D. J. Kresse, Georg, Phys. Rev. B **59**, 1758 (1999).
- ²⁷ J. P. Perdew, K. Burke, and M. Ernzerhof, Phys. Rev. Lett. **77**, 3865 (1996).
- ²⁸ W. Paszkowicz, R. Minikayev, P. Piszora, M. Knapp, C. Bähtz, J. Recio, M. Marques, P. Mori-Sánchez, L. Gerward, and J. Jiang, Phys. Rev. B **69**, 052103 (2004).
- ²⁹ D. M. Ceperley and B. Alder, Physical Review Letters **45**, 566 (1980).
- ³⁰ S. Wei and M. Chou, Physical review letters **69**, 2799 (1992).
- ³¹ Y. Wang, J. Wang, W. Wang, Z. Mei, S. Shang, L. Chen, and Z. Liu, J. Phys.: Condens. Matter **22**, 202201 (2010).
- ³² M. T. Dove, Introduction to lattice dynamics, Vol. 4 (Cambridge university press, 1993) pp. 76–77.
- ³³ A. Ward and D. Broido, Physical Review B **81**, 085205 (2010).
- ³⁴ R. Minikayev, W. Paszkowicz, P. Piszora, M. Knapp, and C. Bähtz, “Thermal expansion of and silicon nitride,” (2007).
- ³⁵ P. Andersson, Journal of Physics C: Solid State Physics **18**, 3943 (1985).
- ³⁶ A. Cepellotti and N. Marzari, Physical Review X **6**, 041013 (2016).
- ³⁷ R. J. Hardy, Physical Review B **2**, 1193 (1970).
- ³⁸ S. Mukhopadhyay, L. Lindsay, and D. J. Singh, Scientific reports **6** (2016).
- ³⁹ A. Kuwabara, K. Matsunaga, and I. Tanaka, Physical Review B **78**, 064104 (2008).
- ⁴⁰ L. Lindsay and D. A. Broido, J. Phys.: Condens. Matter **20**, 165209 (2008).
- ⁴¹ D. C. Wallace, Thermodynamics of Crystals (John Wiley & Sons, Inc., 1972) Chap. 10.